Astron. Astrophys. 338, 191–199 (1998)

ASTRONOMY AND ASTROPHYSICS

# The chromosphere of II Pegasi: multi-line modelling of an RS Canum Venaticorum star

**C.I. Short**[1,2], **P.B. Byrne**[⋆,2], **and P.M. Panagi**[3]

[1] University of Georgia, Department of Physics & Astronomy, Athens, GA 30602-2451, USA (cis@calvin.physast.uga.edu)
[2] Armagh Observatory, College Hill, Armagh BT61 9DG, Northern Ireland
[3] Joint Centre for Mesoscale Meteorology, Reading University, Whiteknights, Reading, RG6 6FN, England

Received 17 March 1998 / Accepted 3 July 1998

**Abstract.** We present the first simultaneous multi-line fitting of a semi-empirical atmospheric model with a chromosphere and transition region to the H I and Ca II spectra of an RS CVn star (II Peg). The static component of the H$\alpha$ emission core, the line profile of H$\beta$, the apparent absence of H$\gamma$ and H$\delta$, and the emission core profiles of Ca II $K$ and two of the Ca II $IR^3$ lines are all approximately fitted by a static $1D$ model with the following properties: $\log m$ at the onset of the transition region is $\approx -2.85$, and a $6000$ K plateau in the upper chromosphere that spans about a decade in $\log m$. In particular, the model is able to reproduce the unusually steep Balmer decrement (compared to the dMe stars), in which H$\alpha$ is strongly in emission and H$\beta$ is in absorption, without recourse to extra-atmospheric material. The Ca II $IR^3$ lines are best fit by a model in which $T_{\min}$ is cooler by 300 K and shallower by over half a decade in $\log m$ than that which best fits the optical lines. The emergent flux in the $IR^3$ line cores arises from the $T_{\min}$ region, whereas the other diagnostics arise from layers well above $T_{\min}$, and it is postulated that this may be the cause of the discrepancy. There has very recently been evidence from other investigators that the metallicity of II Peg may be sub-solar, and we find that models with $[\frac{A}{H}] = -0.4$ provide a somewhat better fit to all the lines considered.

**Key words:** stars: late-type – stars: activity – stars: chromospheres – stars: individual: II Pegasus

## 1. Introduction

RS Canum Venaticorum (RS CVn) systems play a unique role in the study of chromospheric heating in late type stars because their spectra show maximal chromospheric activity for their spectral class. They are post-main sequence stars that are found in close binary systems and are believed to have experienced angular acceleration due to tidal spin-orbit coupling. In the context of the dynamo theory of chromospheric activity, this induced rapid rotation combined with the deepened convection zone of a post-main sequence envelope, is thought to be responsible for their high activity levels (see, for example, Van Buren & Young (1985)).

Relatively strong spectral lines in the visible and near UV spectrum, such as the H I Balmer series and the resonance lines of metals, play an important role in the study of chromospheric and transition region (TR) structure. Their cores form at *relatively* shallow depths where the non-radiative heating dominates, while their wings sample progressively greater depths. Therefore, provided the details of the line formation are understood, they may be used to diagnose the conditions in these outer layers. Eriksson et al. (1983) and papers in that series have demonstrated the diagnostic utility of the Ca II $HK$ line cores for chromospheric modelling in late-type stars over a wide variety of stellar parameters. Houdebine et al. (1995) and Short & Doyle (1997) have developed and demonstrated the diagnostic utility of the H I spectrum for chromospheric modelling of the cooler dM(e) stars, in which H$\alpha$ is strongly in emission as it is in the case of II Peg.

A widely adopted strategy for making use of the diagnostic potential of these lines is to carry out detailed NLTE calculations of radiative transfer in a variety of reasonable chromospheric structures and compare the results with observed profiles. This procedure obviously has uniqueness problems due to the fact that several atmospheric structures that differ significantly from each other may all provide relatively close fits to a particular diagnostic, or a particular type of diagnostic. Nevertheless, by combining several diagnostic lines which sample different portions of the chromosphere and lower transition region, we can gain some measure of confidence in the result. This we attempt to do here for the RS CVn star, II Peg (HD 224085, $V = 7.35$, K2 IV-V), using the first four lines of the HI Balmer series, along with the resonance lines (H&K) and the infra-red triplet ($IR^3$) lines of Ca II. We believe this to be the first time such a calculation has been made for an RS CVn star, although it has been attempted for the active K2 V star $\epsilon$ Eridani (Thatcher et al., 1991).

Furthermore, the attempt to construct a model that can simultaneously fit several such lines with a variety of line formation dependencies is of interest because it tests the extent to which a homogeneous $1D$ model is valid. Recently there has

*Send offprint requests to*: C. I. Short, University of Georgia, Physics and Astronomy, Athens, GA, 30602-2451, USA
⋆ Deceased

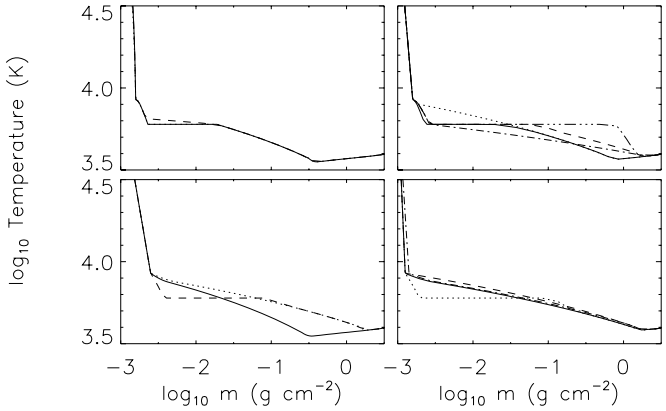


**Fig. 1.** Temperature structure of models in grid. Upper left: Series 1, upper right: Series 2 and 2A, lower left: Series 3, lower right: Series 4.

been increasing evidence that the outer layers of late type stars are highly heterogeneous (see, for example, Ayres 1990).

## 2. Computational method

### *2.1. Atmospheric models*

Fig. 1 shows the upper photosphere, chromosphere and lower TR of a grid of fifteen atmospheric models that were used in the present study. These models have as their photospheric base a radiative equilibrium model that was found by interpolation between two models taken from the grid of Kurucz (1992). This photospheric model corresponds to a star of $T_{\rm eff} = 4600$ K, log $g = 3.5$, $[\frac{A}{H}] = 0.0$, and $\xi_{\rm T} = 2.0$ km s$^{-1}$. This value of $T_{\rm eff}$ is slightly cooler than the value of $4650$ K found by Byrne et al. (1995) for the unspotted photosphere of II Peg from an analysis of the light curve. However, the precise value is probably uncertain by $\pm$100 K due to, among other things, uncertainties in accounting for starspots effects. The value of $\log g$ is at the lower end of the range found by Vogt (1981) from an estimate of the stellar radius based on a measure of $v \sin i$ and an estimate of $i$. Nevertheless, these parameters should be sufficiently accurate for our purpose of investigating the chromospheric structure.

Onto the base photosphere we have added a set of chromosphere and TR temperature structures that cover a range of values of $T_{\rm min}$ and $m_{\rm TR}$, where $m_{\rm TR}$ designates the value of the column mass density, $m$, at the onset of the transition region at the top of the chromosphere. The TR extends to a temperature of $100\,000$ K. The grid explores various functional forms of $T$ versus $m$ in the chromosphere. Table 1 shows the values of these model parameters for each model in the grid. Following Ayres (1979), all models have $T(m_{\rm TR})$, the temperature at the top of the chromosphere, equal to $\approx 8000$ K. Because the atmosphere below $T_{\rm min}$ is close to radiative equilibrium (RE), the choice of $T_{\rm min}$ fixes the value of $m_{\rm Tmin}$, the location of $T_{\rm min}$ in column mass density. The grid also spans a range in the thickness of the TR and the functional form of $T(m)$ in the TR. Because of the *ad hoc* nature of micro-turbulent velocity ($\xi_{\rm T}$), we have chosen to set $\xi_{\rm T} = 0$ throughout our model as a first approximation. The structure of the underlying photospheric model has been computed taking into account the effect of line blanketing opacity in which the lines have a Doppler core width corresponding to $\xi_{\rm T} = 2.0$ km s$^{-1}$. However, weak, narrow photospheric lines on the linear part of the curve of growth in our computed non-LTE spectra will be too narrow due to the neglect of photospheric micro-turbulence.

**Table 1.** Parameters of grid models

| Model | $m_{\rm TR}$ | TR $\frac{dT}{d\log m}$ | $m_{\rm Tmin}$ | $T_{\rm min}$ | Chromos. $\frac{dT}{d\log m}$ |
|---|---|---|---|---|---|
| Series 1 | | | | | |
| 1 | -2.8 | $-6.2\times10^5$ | -0.4 | 3550 | variable |
| 2 | -2.8 | $-5.1\times10^5$ | -0.4 | 3550 | variable |
| 3 | -2.8 | $-6.2\times10^5$ | -0.4 | 3590 | variable |
| Series 2 | | $\frac{d\log T}{d\log m}$ | | | |
| 4 | -2.8 | $-5.4$ | -0.1 | 3690 | variable |
| 5 | -2.8 | $-5.4$ | -0.1 | 3690 | -1600 |
| Series 2$A$ | | | | | |
| 6 | -2.8 | $-5.4$ | 0.24 | 3870 | variable |
| 7 | -2.8 | $-5.4$ | 0.33 | 3900 | -750 |
| 8 | -2.8 | $-5.4$ | 0.2-0.4 | 3850 | variable |
| Series 3 | | | | | |
| 9 | -2.6 | $-2.7$ | -0.5 | 3520 | -2100 |
| 10 | -2.6 | $-2.7$ | 0.1 | 3830 | -1400 |
| 11 | -2.6 | $-2.7$ | 0.1 | 3860 | variable |
| Series 4 | | | | | |
| 12 | -2.9 | $-10.7$ | 0.25 | 3870 | -1300 |
| 13 | -2.9 | $-10.7$ | 0.25 | 3850 | variable |
| 14 | -2.9 | $-10.7$ | 0.25 | 3880 | -1500 |
| 15 | -2.85 | $-10.7$ | 0.25 | 3870 | -1300 |

The range of values of $m_{\rm TR}$ covered by the grid corresponds to a range in the value of the chromospheric pressure, which is a determinant of the strength of spectral chromospheric activity level indicators. The range of values of the difference $m_{\rm TR} - m_{\rm Tmin}$ covered by the grid corresponds to a range of values of the chromospheric thickness, or, equivalently, the mean steepness of the chromospheric gradient.

For clarity, the grid has been divided into four series of models, each characterized by common properties: Series 1 models have $m_{\rm TR} = -2.8$, $m_{\rm Tmin} \approx -0.4$, and constant $(d{\rm T}/d\log m)_{\rm TR}$; Series 2 models have $m_{\rm TR} = -2.8$, $m_{\rm Tmin} \approx -0.1$, and constant $(d\log T/d\log m)_{\rm TR}$; Series 2$A$ models also have $m_{\rm TR} = -2.8$, constant $(d\log T/d\log m)_{\rm TR}$, and various values of $m_{\rm Tmin}$; Series 3 has models of higher chromospheric pressure with $m_{\rm TR} = -2.6$, $m_{\rm Tmin} \approx -0.1$, and constant $(d\log T/d\log m)_{\rm TR}$; Series 4 has models of lower chromospheric pressure with $m_{\rm TR} = -2.9$, $m_{\rm Tmin} \approx 0.25$, and constant $(d\log T/d\log m)_{\rm TR}$. Within each series are various functional forms for the chromospheric $d{\rm T}/d\log m$, some of which include an upper chromosphere plateau.

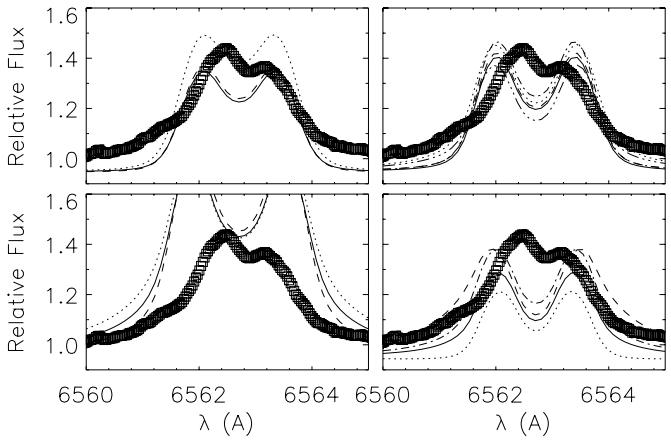


**Fig. 2.** Observed and computed H$\alpha$ line profiles. Observed profile (squares). Upper left- Series 1: Model 1 (solid line), model 2 (dotted line), model 3 (dashed line); upper right- Series 2 and 2A: Model 4 (solid line), model 5 (dotted line), model 6 (dashed line), model 7 (dot-dashed line), model 8 (dot-dot-dot-dashed line); lower left- Series 3: Model 9 (solid line), model 10 (dotted line), model 11 (dashed line); lower right- Series 4: Model 12 (solid line), model 13 (dotted line), model 14 (dashed line), model 15 (dot-dashed line).

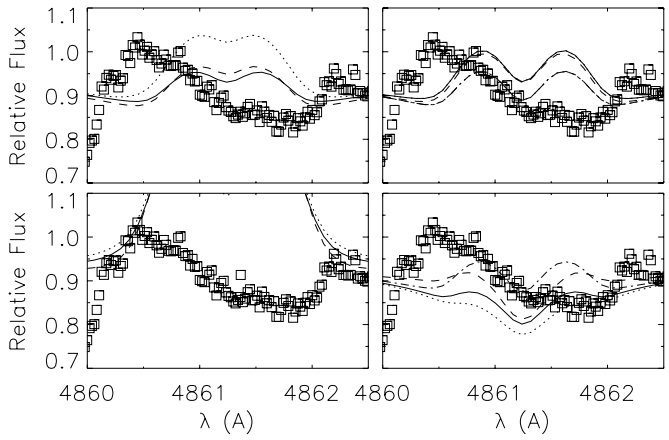


**Fig. 3.** Observed and computed H$\beta$ line profiles. See Fig. 1 caption.

### *2.2. Atomic models*

#### 2.2.1. NLTE Hydrogen

We have used version 2.2 of the code MULTI (Carlsson 1986) to solve the combined radiative transfer and statistical equilibrium equations for an atomic model that incorporates the lowest nine levels of H I and the H II state. Because the chromospheric $N_{\rm e}$ density structure is determined to a significant extent by the H I/H II ionization balance, we iterate the non-LTE solution and the equation of hydrostatic equilibrium to convergence. The radiative transfer problem is solved in detail for all $36$ $b-b$ transitions connecting the nine H I states and for the $b-f$ transitions of these states. Collisional transitions due to electrons are taken in to account for all transitions.

The Ly$\alpha$ line has an significant effect on the statistical equilibrium of H I. We treat the Lyman series lines as pure Doppler cores to approximate the effect of Partial Frequency Redistribution (PRD) of line photons, a procedure that has been found to be adequate in the case of the Sun (Lites 1987).

#### 2.2.2. NLTE Calcium

We use a version of MULTI that has been generalized to include the effect of PRD in the transfer of line photons (Uitenbroek 1989) to solve simultaneously the coupled radiative transfer and statistical equilibrium equations for an atomic model that incorporates eight states of Ca I, the lowest five states of Ca II, and the ground state of Ca III. Ten $b-b$ and thirteen $b-f$ transitions are treated in detail. Collisional excitations and ionizations among all levels due to electrons are included. All atomic data are those compiled and presented by Drake (1991), except for Stark broadening parameters taken from Thatcher et al. (1991), and have been found to provide a good fit to the solar Ca II $HK$ and $IR^3$ line profiles. The treatment of Van der Waals damping in MULTI has been modified by Panagi (1990) to use the treatment of Derrider and van Rensbergen (1976) for the strong Ca II lines. The Ca II $HK$ doublet connects the $4s^2S$ ground state to the double $4p^2P$ ($25340$ cm$^{-1}$) state. In turn, the $4p^2P$ state is connected to the lower energy metastable double $3d^2D$ ($13682$ cm$^{-1}$) state by the $IR^3$ lines. The effect of PRD is accounted in both the $HK$ doublet and the $IR^3$ lines.

The Ca calculation incorporates the non-LTE $N_{\rm e}$ structure produced by the H I/II calculation. The ground state ionization energies of Ca I and Ca II are $6.11$ eV and $17.98$ ev, respectively. As a result, Ca II forms the reservoir population throughout most of the photosphere and chromosphere, except for the transition region where the reservoir shifts to Ca III. Therefore, the level populations in the Ca II stage are relatively insensitive to the details of the ionization balance.

The synthetic flux profiles were convolved with a function to account for the rotational broadening of $v \sin i = 21$ km s$^{-1}$ (Vogt 1981) and the instrumental resolution of the corresponding observed profile.

## 3. Results and discussion

### *3.1. The Hydrogen spectrum*

The mean H$\alpha$ and H$\beta$ spectra (Figs. 2 and 3) were derived from spectra taken in 1991 with the QUBES spectrograph ($R = 56\,000$) at the 1m Jacobus Kapteyn Telescope (JKT) at the Observatorio del Roque de los Muchachos. H$\gamma$ and H$\delta$ spectra were also obtained in 1991 with the Penn State Fiber Optic Echelle Spectrograph (FOE) ($R = 12\,000$) on the Kitt Peak National Observatory coudé feed telescope. Both data sets were originally presented and described by Byrne et al. (1995), to which the reader is referred for details.

Byrne et al. (1995, 1998) have shown that, in spite of considerable short-term variability, the *mean* H$\alpha$ profile of II Peg shows remarkable stability over time. They found that the time averaged profile, shown in Fig. 2, can be described by two distinct Gaussian components, each with a different velocity in the rest frame of the star. One component describes the emission

core and the other describes the central absorption self-reversal. The velocity separation of these two components is constant. However, the strength of the central reversal is variable, which leads to a variable asymmetry in the emission peaks. There is also a variable emission component in the wings in addition to the Gaussian wings of the main emission core. The time scale of the variability is that of the stellar rotation period. Byrne et al. (1995) hypothesize that the time variability of the overall profile may be explained by spicule-like velocity outflows and inflows, but a detailed model of the velocity field that can account of the observed variability is lacking. The FWHM of the emission core is constant with time and reflects the conditions in the mean chromosphere. Therefore, we expect that the static models in our grid will only be able to reproduce the width of the emission core.

The observed mean H$\beta$ line is shown in Fig. 3. The EW of this line shows time variability of similar amplitude and time scale to that of H$\alpha$. However, because of its weakness the variability results in the line switching between weak absorption and weak emission. The red wing is severely blended with strong photospheric absorption lines. Therefore, we expect to be able to fit only the blue wing. Another feature of note is the extremely steep Balmer decrement, with H$\alpha$ being strongly in emission and H$\beta$ in absorption. The steepness of the decrement relative to other late type stars has been cited as evidence that the H I spectrum may be dominated by material of a non-atmospheric or extra-atmospheric origin (Huenemoerder & Ramsey 1987).

Fig. 2 shows the synthetic H$\alpha$ line profiles for the grid of models. The general variation in the synthetic H$\alpha$ and H$\beta$ line profiles with chromospheric parameters follows that found in previous investigations of emission line formation in active atmospheric models of dM stars, such as that by Houdebine et al (1995) and Short & Doyle (1997). *To wit:* a general increase in both the $FWHM$ of the emission core and value of the flux at line center, $F_\nu(\Delta\lambda = 0)$, as the value of $m_{\rm Tmin}$ and $m_{\rm TR}$ increase, and an increase in the depth of the central absorption reversal as the TR becomes thicker in $\log$ column mass. A detailed discussion of the line formation in a chromospheric model can be found in these studies. The moderate $S/N$ of the observed spectra does not allow detailed comparison with synthetic profile. However, several general points of comparison can be made.

Model 12 from Series 4 gives the closest fit to the FWHM of the H$\alpha$ line, although the peak flux is too low. This model also gives a good match to the shape of the unblended blue wing of the H$\beta$ line. All the models produce H$\alpha$ profiles in which the separation of the emission peaks is too large. However model 13 from Series 4 gives the closest fit to the peak separation, although the FWHM is too small. This model yields an H$\beta$ profile that is close to that observed, but slightly too strong. Model 1 from Series 1 yields an H$\alpha$ profile that gives a good match to both $F_\nu(\Delta\lambda = 0)$ and $F_\nu$ in the emission peaks, but the FWHM is too large. This model gives an H$\beta$ profile that is grossly discrepant with the observed profile. All of the models , with the exception of model 10, produce flux in the wings of H$\alpha$ that is much smaller than that observed.

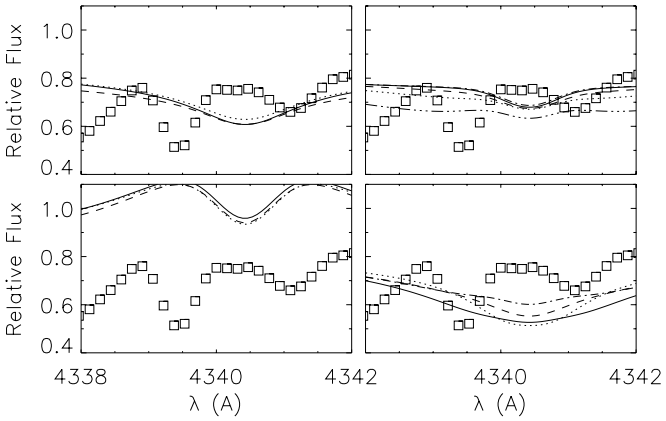


**Fig. 4.** Observed and computed H$\gamma$ line profiles. See Fig. 1 caption.

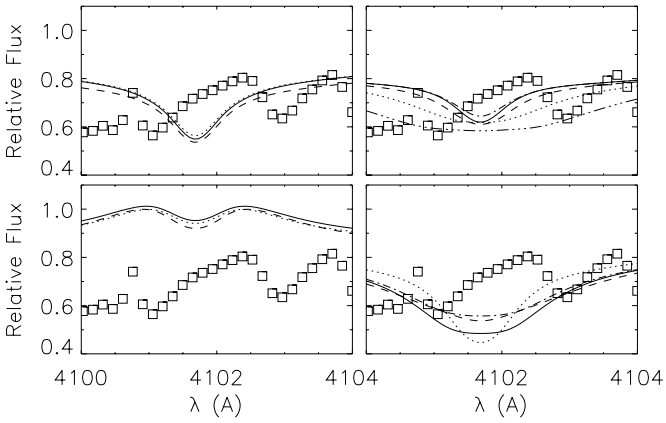


**Fig. 5.** Observed and computed H$\delta$ line profiles. See Fig. 1 caption.

In light of the time variability and mean profile analysis of Byrne et al. (1995) that was discussed above, we expect that the width of the emission core is the only feature of the observed H$\alpha$ profile that may be meaningfully fit by a static model. On this basis, and on the basis of its ability to fit the H$\beta$ line, we conclude that model 12 from Series 4, which is the series of low chromospheric pressure models, gives the best fit to the hydrogen spectrum. We note that this model is able to account for the steep Balmer decrement with a conventional $1D$ hydrostatic atmospheric model.

Figs. 4 and 5 show the comparison between the observed and computed H$\gamma$ and H$\delta$ regions. The apparent weakness of the Balmer series above H$\beta$ and the severe overblanketing due to background line opacity in the blue spectral region conspire to make both of these lines undetectable by casual visual inspection. The only conclusion that we draw from the observed spectrum is that these lines are very weak. Most of the models in the grid give rise to synthetic profiles that are broad and shallow, and which, if present in the observed spectrum, might be obscured by the heavy line blanketing. Therefore, we conclude that the models are not inconsistent with the observed spectrum in the region of H$\gamma$ and H$\delta$. However, it is disturbing that model 13, which gives one of the best simultaneous fits to H$\alpha$ and H$\beta$,

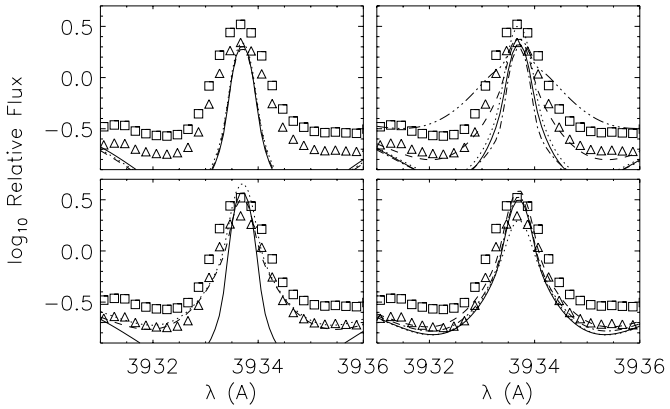


**Fig. 6.** Observed and computed Ca II $K$ line profiles: emission core. See Fig. 1 caption. Squares and triangles represent two different continuum rectifications of the observed spectrum (see text).

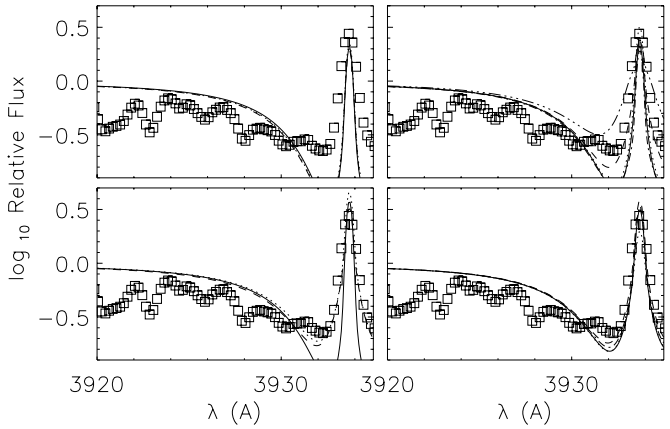


**Fig. 7.** Observed and computed Ca II $K$ line profiles: blue wing. See Fig. 1 caption.

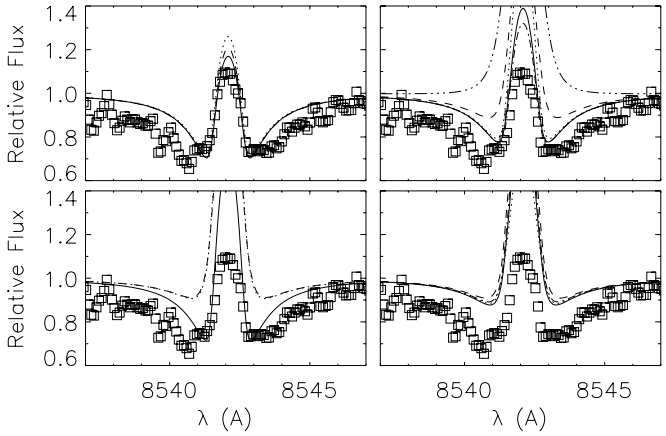


**Fig. 8.** Observed and computed Ca II 8542 line profiles. See Fig. 1 caption.

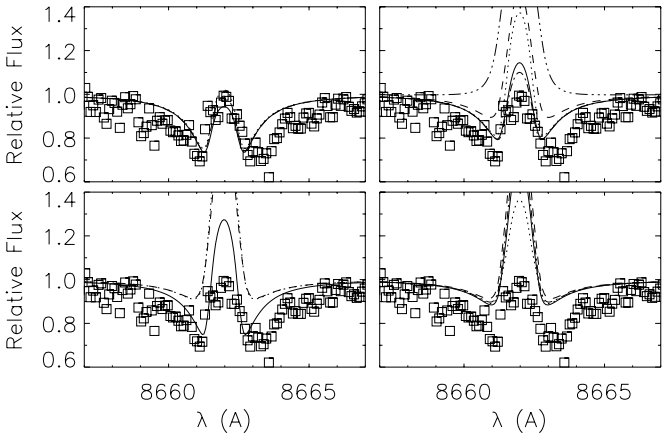


**Fig. 9.** Observed and computed Ca II 8662 line profiles. See Fig. 1 caption.

gives rise to the narrowest and deepest, and, therefore, most discrepant, predicted H$\delta$ line.

### *3.2. The Ca* II *spectrum*

The Ca II $HK$ spectrum was obtained in 1991 with the FOE spectrograph at KPNO as part of the same observing program at which the H$\gamma$ and H$\delta$ spectra were obtained (Byrne et al. 1995). The Ca II $IR^3$ $\lambda$8542 and 8662 spectra were taken with the MUSICOS spectrograph ($R =\sim 35\,000$) on the 2m telescope at the Observatoire du Pic du Midi by Dr. C. Catalá (Observatoire de Meudon) (Byrne et al. 1998). These papers present a detailed discussion of the observations. Figs. 6 and 7 show the observed and computed Ca II $HK$ line core and wing profiles. Figs. 8 and 9 show the observed and computed Ca II $\lambda$8542 and $\lambda$8662 lines. Because of the large uncertainty in the background subtraction and flux calibration, the Ca II $K$ spectrum is uncertain in relative flux by $\approx 20\%$. Therefore, we have plotted the upper and lower uncertainty limits for this line.

As with H I, the general response of the computed Ca II line profiles to changes in chromospheric parameters is consistent with the results of previous chromospheric modelling of these lines, such as those of Eriksson et al (1983): an increase in the separation, $\Delta\lambda$, of the $K_1$ flux minimum points on either side of the central emission reversal as the value of $m_{\rm Tmin}$ increases, an increase of the value of the flux, $F_\nu(K_1)$ at these points as the value of $T_{\rm min}$ increases, and an increase in the value of the flux *contrast* between $F_\nu(\Delta\lambda = 0)$ and $F_\nu(K_1)$ as $m_{\rm TR}$ increases. Note that *at this spectral resolution*, these models differ from the solar case in that they do not show the doubly reversed core with a central absorption component that gives rise to double emission peaks. Fig. 7 shows that all the models provide an approximate fit to the overall shape of the far wings of these heavily damped photospheric lines. This indicates that the photospheric model is a close representation to the mean photosphere of II Peg.

The spectral resolution is too low to resolve the distinctive double peaked emission core of Ca II $K$, if present in this star. However, all the models in Series 3 and 4 with the exception of model 8 provide close fits to the FWHM of the emission core, although all are too narrow. Model 13 in Series 4 provides the closest fit to the ratio of the FWHM to $F_\nu(\Delta\lambda = 0)$, thereby providing the best match to the overall shape of the $K$ emission

core, although it is slightly too weak. Of the models in these two series, model 10 from Series 3 and model 11 from Series 4 give the best fit to $F_\nu(\Delta\lambda = 0)$. The separation and brightness of the $K1$ points where the line turns over into emission are critical diagnostics of the $m_{\rm Tmin}$ and $T_{\rm min}$, respectively. The $K1$ separation is approximately fitted by almost all the models. However, the brightness of the $K1$ points is matched only by models in Series 3 and 4 and by model 6 in Series 2. The models in Series 1 all give rise to approximately the same $IR^3$ line profiles, which provides the closest match to the observed emission cores of both lines.

### *3.3. The multi-line fit*

Model 13 in Series 4 provides a relatively close fit to both the H I Balmer spectrum and the Ca II $K$ line. Among the grid models, those of Series 4 have the lowest chromospheric pressure, the deepest $T_{\rm min}$ location, and the thickest chromosphere with the shallowest chromospheric $T$ gradient. By contrast, all the Series 4 models are grossly discrepant with the observed Ca II $IR^3$ spectrum. The $IR^3$ lines are best fitted by models of Series 1, which have intermediate chromospheric pressure, a relatively shallow $T_{\rm min}$ location, and a relatively steep $T$ gradient in the lower chromosphere.

We note that model 13 and the models is Series 1 all have a 6000 K $T$ plateau in the upper chromosphere that starts in the middle chromosphere and extends to the TR. Also, the range in chromospheric pressure, specified by the value of $m_{\rm TR}$, spanned by the grid is relatively narrow, with model 13 differing from the Series 1 models by only 0.1 in $\log m_{\rm TR}$. Models of Series 1 and 4 both have a TR thickness of $\approx 0.15$ in log column mass density. However, the two series have different functional forms for $T(m)_{\rm TR}$, with Series 1 having constant $d{\rm T}/d\log m$ and Series 4 having constant $d\log T/d\log m$. Therefore, all five lines in this study are best matched by models having approximately the same upper chromosphere and TR structure.

It is worth noting that models 12 and 14 from Series 4, neither of which have a chromospheric $T$ plateau, also provide a very good fit to the blue wing of H$\beta$ and are not very discrepant with either H$\alpha$ or Ca II $K$. In fact, model 14 provides a particularly close match to the FWHM of the $K$ line emission core. The approximate match provided by these two models qualifies the choice of model 13 as the best fit to the Balmer spectrum and the Ca II $K$ line. However, it also re-enforces the conclusion that Series 4 best represents the outer atmosphere of II Peg. Also model 10 from Series 3 fits the unusually bright emission wings of H$\alpha$ and provides a good fit to the FWHM and $F_\nu(\Delta\lambda = 0)$ of the $K$ line core.

Fig. 10 shows the monochromatic source function, $S_\nu$, and the *flux* contribution function, $C_{\rm F}$, at $\Delta\lambda \approx 0$ and at a critical value of $\Delta\lambda$ in the line wing for all the line diagnostics for model 13. The Planck function, $B_\nu$, is also shown for reference. For H$\alpha$, these quantities are shown only for the FWHM point in the emission core at $\Delta\lambda = 0.84A$, which is the only part of the variable H$\alpha$ profile that may be used as a diagnostic of the mean atmosphere. For clarification, we note that the *line*

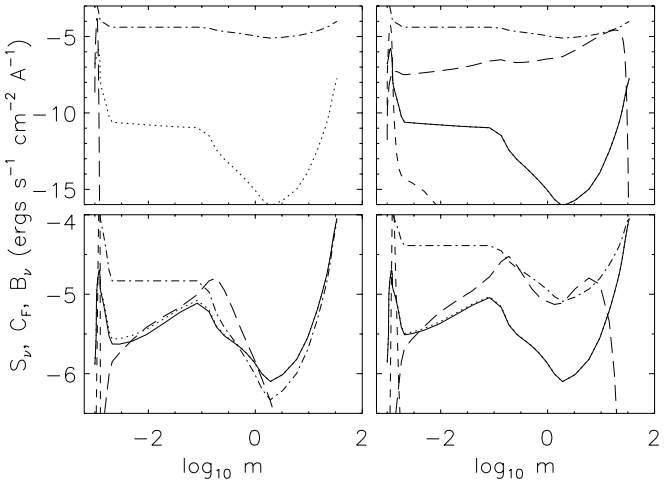


**Fig. 10.** Radiative transfer quantities at critical $\Delta\lambda$ values of the line diagnostics. Solid line: $S_\nu$ in line core; dotted line: $S_\nu$ in line wing or FWHM point (see text); short dashed line: $C_{\rm F}$ in line core; long dashed line: $C_{\rm F}$ in line wing or FWHM point; Dot dashed line: $B_\nu$. Upper left: H$\alpha$; Upper right: H$\beta$; lower left: Ca II $K$; lower right: Ca II 8662.

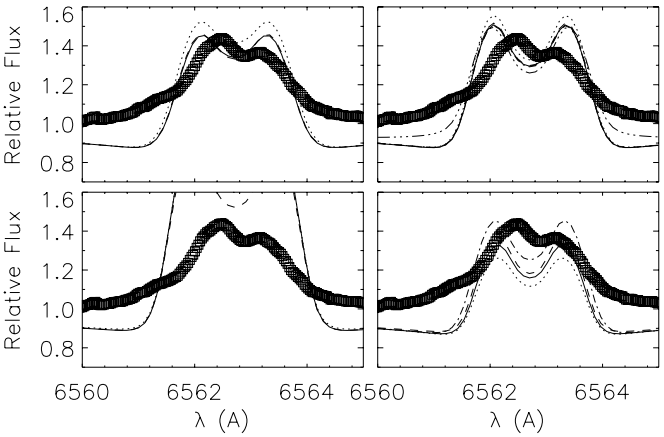


**Fig. 11.** Observed and computed H$\alpha$ line profiles for models with $[\frac{A}{H}] = -0.4$. See Fig. 1 caption.

source function, $S_{\rm l}$, as typically defined by, for example, Mihalas (1978), is the same throughout a particular H I line because the H I transitions are treated in CRD. However, the emergent flux is the sum of the *total* source function along the lines of sight weighted by $C_{\rm F}$. The total monochromatic source function, $S_\nu$, is the weighted sum of $S_{\rm l}$ and the background source function, $S_{\rm c}$, due to overlapping continuum transitions. The value of $S_{\rm c}$ is approximately constant over the narrow $\Delta\lambda$ interval of a line profile. However, the relative contributions of $S_{\rm l}$ and $S_{\rm c}$ to the value of $S_\nu$ will change considerably throughout the line profile as the ratio of line opacity to background opacity changes. Therefore, $S_\nu$ will vary throughout the line profile. For Ca II $K$ and $\lambda$8662, the line wing quantities are shown for the $K1$ point and the corresponding point in the $\lambda$8662 line (*ie* flux minimum points) at $\Delta\lambda = 1.3$ A and 0.6 A, respectively. For H$\beta$, the wing point is at $\Delta\lambda = 0.16$ A.

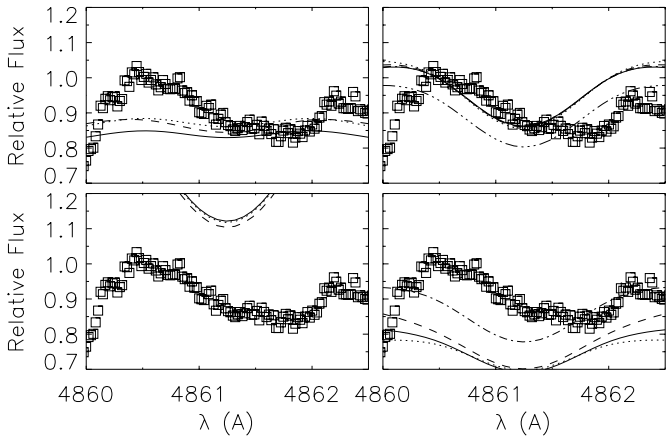


**Fig. 12.** Observed and computed H$\beta$ line profiles for models with $[\frac{A}{H}] = -0.4$. See Fig. 1 caption.

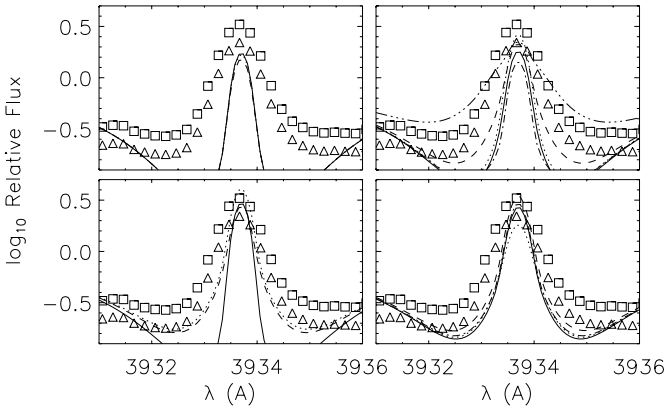


**Fig. 13.** Observed and computed Ca II $K$ line profiles for models with $[\frac{A}{H}] = -0.4$. See Fig. 1 caption.

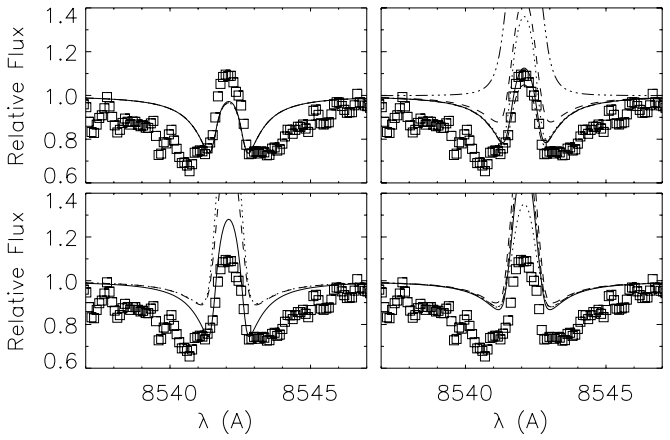


**Fig. 14.** Observed and computed Ca II 8542 line profiles for models with $[\frac{A}{H}] = -0.4$. See Fig. 1 caption.

Comparison of $C_{\rm F}$ among the various diagnostics may provide a clue as to why the Ca II $IR^3$ lines correspond to a different lower chromospheric structure than the other lines. For the H$\alpha$ FWHM point, H$\beta$ $\Delta\lambda \approx 0$, and the Ca II $K$ $\Delta\lambda \approx 0$ and $K1$ points $C_{\rm F}$ either peaks sharply in the upper chromosphere or lower TR, or is more heavily weighted toward the upper chromosphere than to any other part of the atmosphere. Therefore, for these diagnostics the emergent flux, $F_\nu(\tau = 0)$, samples the outermost layers. In the case of the H$\beta$ wing point, $C_{\rm F}$ is broadly distributed throughout the atmosphere, but has a definite peak near the bottom of the photosphere. Therefore, the chromospheric structure does not greatly influence $F_\nu(\tau = 0)$. By contrast, $C_{\rm F}$ in the Ca II 8662 flux minimum point has a significant local peak near $T_{\rm min}$. Therefore, $F_\nu(\tau = 0)$ here samples the lower chromosphere and upper photosphere more heavily than any of the other diagnostics in the study. However, $C_{\rm F}$ at $\Delta\lambda \approx 0$ in this line, as in the case of the other lines, peaks in the upper chromosphere. Nevertheless, the net effect on the broadened Ca II 8662 line core is that it is more strongly sensitive to lower chromospheric structure than any of the other lines.

### *3.4. The effect of metallicity*

It is significant that the unusually steep Balmer decrement from the strong H$\alpha$ emission line to the weak H$\beta$ absorption line can be entirely accounted for by a conventional atmospheric structure without recourse to extra-atmospheric plasma. As we were concluding the present investigation, we became aware that Berdyugina et al. (1998) have presently found evidence that the metallicity of II Peg may be significantly sub-solar, with $[\frac{A}{H}] = -0.4$. To test how robust our Balmer decrement result is against perturbations to the background opacity, we have attached our grid of chromosphere/*TR* structures to a photospheric model with $[\frac{A}{H}] = -0.4$ taken from the grid of Kurucz (1992). For these models we recomputed the H I/II radiative transfer and statistical equilibrium with background opacity corresponding to $[\frac{A}{H}] = -0.4$. Metallicity effects may be significant in early K sub-giants because, in addition to the direct effect on the opacity, Hydrogen is mostly neutral in the upper photosphere and lower chromosphere and metals are the dominant electron contributor.

Figs. 11 and 12 show the recomputed H$\alpha$ and H$\beta$ profiles. Both lines are significantly affected by the reduced metallicity. The H$\alpha$ emission core becomes stronger with the result that all models, with the possible exception of Models 12, 13, and 14 in Series 4, are now too bright. model 13 still provides the closest fit. Interestingly, the central absorption reversal is weaker when the metallicity is reduced, which yields profiles that more closely resemble the observed one.

The weak emission reversal predicted for the H$\beta$ line with the Series 2 and 4 models completely disappears when the metallicity is reduced. The Series 1 models give rise to flat profiles that seem to be almost exactly balanced between emission and absorption. Interestingly, despite the radical change in the shape of the H$\beta$ profile to pure absorption, the Series 2 and 4 models, including model 13, still predict the correct slope for the blue wing, and some of the Series 2 models also predict the correct flux level. The predicted steepness of the Balmer decrement is

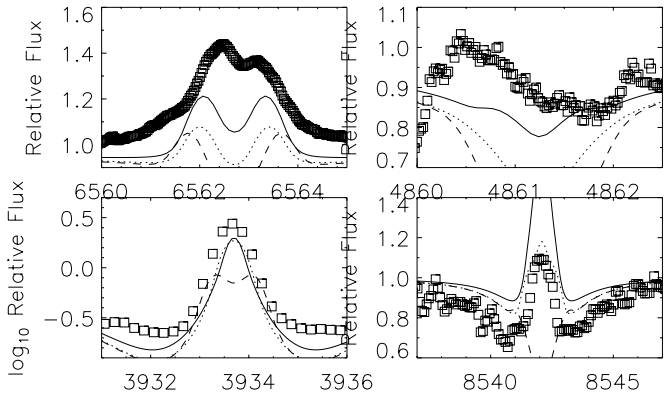


**Fig. 15.** Observed and computed line profiles with three different $\xi_{\rm T}(m)$ distributions. Solid line: $\xi_{\rm T} = 0$ km s$^{-1}$, dotted line: $\xi_{\rm T} = 5$ km s$^{-1}$, dashed line $\xi_{\rm T} = 5$ km s$^{-1}$ in the photosphere and increasing linearly with $\log m$ to 15 km s$^{-1}$ at the base of the *TR*. Top left panel: H$\alpha$, top right panel: H$\beta$, lower left panel: Ca II $K$, lower right panel: Ca II 8542.

even greater in the case of $[\frac{A}{H}] = -0.4$, and, arguably, model 13 still provides the best simultaneous fit to the H I spectrum.

Figs. 13 and 14 show the predicted Ca II $K$ and 8542 lines for the models with $[\frac{A}{H}] = -0.4$. The inner wings of the predicted Ca II $K$ line are slightly darker, which seems to worsen the overall fit. However, the predicted chromospheric core emission profiles are almost identical to those computed with solar metallicity models. Interestingly, the predicted strength of the Ca II 8542 emission core is reduced, which brings model 13 into much closer agreement with the observed spectrum, although the discrepancy is still significant. Nevertheless, the closest simultaneous fit to *all* lines in this investigation seems to be found among the reduced metallicity models.

### *3.5. The effect of turbulent velocity*

Because the physical significance of a turbulent velocity in the atmospheric model is unclear to us, we chose to set $\xi_{\rm T} = 0$ for this initial modelling attempt. However, historically, the chromospheric modelling of a wide variety of late type stars has been moderately successful with the inclusion of non-zero $\xi_{\rm T}$ values. The photospheric models of late type dwarfs of Kurucz (1992) typically have $\xi_{\rm T} = 2$ km s$^{-1}$, and, generally, $\xi_{\rm T}$ correlates positively with luminosity class (see, for example, Gray 1990). Therefore, we chose a photospheric value of $\xi_{\rm T} = 5$ km s$^{-1}$ and recomputed the line profiles for our best fit model with two depth distributions of $\xi_{\rm T}$: one in which $\xi_{\rm T}(m)$ is constant throughout the entire atmosphere, and one in which $\xi_{\rm T}(m)$ increases linearly with $\log m$ throughout the chromosphere from the photospheric value to a value of 15 km s$^{-1}$ at the base of the *TR*. The latter functional dependence on $\log m$ was chosen because such a depth distribution has been used successfully in the modelling of a variety of late-type stars (see, for example, Eriksson et al. (1983), Basri et al. (1981) and other papers in that lineage).

Fig. 15 shows the observed line profiles for H$\alpha$, H$\beta$, Ca II $K$, and Ca II 8542 and the computed line profiles with three different $\xi_{\rm T}(m)$ distributions; the two described above, and $\xi_{\rm T} = 0$ km s$^{-1}$. With the exception of Ca II $K$ in the case where $\xi_{\rm T} = 5$ km s$^{-1}$ everywhere, there is a general tendency for non-zero $\xi_{\rm T}$ to decrease the relative brightness of the chromospheric emission cores. In all cases, non-zero $\xi_{\rm T}$ decreases the flux in the line wings. We note that in the case of H$\alpha$, a model in which $\xi_{\rm T}$ increases throughout the chromosphere has emission peaks that are separated by a greater value of $\Delta\lambda$ than does a model with small or zero chromospheric $\xi_{\rm T}$ values. This well known effect arises because the peaks form in the upper chromosphere where the Doppler broadening due to the local value of $\xi_{\rm T}$ is greater in such a model. The H$\beta$ line is especially sensitive to $\xi_{\rm T}$, going from weak absorption with very weak emission wings, to strong absorption in the presence of non-zero $\xi_{\rm T}$ values.

With the exception of Ca II 8542 in the case where $\xi_{\rm T}(m) = 5$ km s$^{-1}$ everyhere, the ability of model 13 to fit the observed spectrum is worsened by the adoption of non-zero $\xi_{\rm T}$, although the effect on the Ca II $K$ emission core of adopting $\xi_{\rm T}(m) = 5$ km s$^{-1}$ everywhere is almost negligible. We must point out that if the synthetic line profiles were re-computed for the entire model grid with an ideal choice of $\xi_{\rm T}(m)$ it is possible, but not certain, that one model could simultaneously fit *all* of the observed lines well.

## 4. Conclusion

This is the first attempt that we are aware of to fit a chromospheric/TR atmospheric model to multiple lines in the spectrum of an active *subgiant*. To a first approximation, all the lines included in this study are best fitted by the same upper chromospheric structure with a 6000 K plateau that spans $\approx 1$ g cm$^{-2}$ at the top of the chromosphere and $m_{\rm TR} \approx -2.85$. However, the lines are discrepant in their match to the lower chromosphere, with the optical lines being best fitted by a model in which $m_{\rm min}$ is larger by $\approx 0.65$ g cm$^{-2}$ and $T_{\rm min}$ is hotter by $\approx 300$ K than those of the model that best fits the IR lines. The discrepancy may be due to a dichotomy in the detailed line formation of the H$\alpha$ emission core, the H$\beta$ core and the inner Ca II $K$ profile on one hand, and the Ca II $IR^3$ lines on the other; the two sets of lines are most sensitive to different parts of the outer atmosphere, and there is no one model in our grid that has both the correct lower and correct upper atmospheric structure.

We note that the unusually steep Balmer decrement, with strong H$\alpha$ emission and weak H$\beta$ absorption, can be entirely reproduced with a conventional $1D$ hydrostatic atmospheric structure. The only difference between these models and those of active dwarfs in which the entire Balmer series behaves en mass is the lower value of $\log g$ that corresponds to a subgiant. The steepness of the Balmer decrement with respect to that for active dwarfs is entirely due to the effect of the slightly lower surface gravity on the formation of the spectrum. Furthermore, the steep Balmer decrement is insensitive to modest changes in the value of the metallicity.

We draw special attention to the large sensitivity of the predicted H$\alpha$, H$\beta$, and Ca II 8542 line profiles to a modest change in the metal abundance. This result indicates that the outer atmospheric structure that is inferred from the H I and Ca II spectra may be highly dependent on the value of $[\frac{A}{H}]$. Given that a subsolar value for $[\frac{A}{H}]$ has just been found for II Peg by Berdyugina et al. (1998), and is uncertain, or has never been measured for other active late-type stars, a degree of caution is called for. We note that the model that came closest to providing a simultaneous fit to all the H I and Ca II lines in this study was one with $[\frac{A}{H}] = -0.4$

*Acknowledgements.* Research at Armagh Observatory is supported by a Grant-in-Aid from the Department of Education for Northern Ireland. CIS was supported by PPARC Research Grant GR/K04613. We also acknowledge support at Armagh in terms of both software and hardware by the STARLINK Project, funded by the UK PPARC. We are indebted H. Uitenbroek for access to the PRD version of MULTI.

## References

Ayres, T. R., 1990, in IAU Symposium 138, Solar Photosphere: Structure, Convection, and Magnetic Fields., ed. J. O. Stenflo (Dordrecht: Kluwer), p. 23
Ayres, T. R., 1981, ApJ, 244, 1064
Ayres, T. R., 1979, ApJ, 228, 509
Basri, G. S., Linsky, J. L., & Eriksson, K., 1981, ApJ, 251, 162
Berdyugina, S., Jankov, S., Ilyin, I., Tuominen, I., & Fekel, F. C., 1997, A&A, 334, 863
Byrne, P. B., Panagi, P. M., Lanzafame, A. C., Avgoloupis, S., Huenemoerder, D. P., Kilkenny, D., Marang, F., Panov, K. P., Roberts, G., Seiradakis, J. H., & van Wyk, F., 1995a, A&A, 299, 115
Byrne, P.B., Abdul Aziz, H., Amado, P.J., Arevalo, M.J., Avgoloupis, S., Doyle, J.G., Eibe, M.T., Elliott, K.H., Jeffries, R.D., Lanzafame, A.C., Lazaro, C., Murphy, H.M., Neff, J.E., Panov, K.P., Sarro, L.M., Seiradakis, J.H., Spencer, R.E., 1998, A&AS, 127, 505
Carlsson, M., 1986, Uppsala Observatory Internal Report no. 33
Derrider, G. & van Rensbergen, W., 1976, A&A, 23, 147
Drake, J. J., 1991, MNRAS, 251, 369
Eriksson, K., Linsky, J. L., & Simon, T., 1983, ApJ, 272, 665
Gray, D. F., 1988, Lectures on Spectral-Line Analysis: F,G, and K Stars, (ESO)
Houdebine, E. R., Doyle, J. G., & Koscielecki, M., 1995, A&A, 294, 773
Huenemoerder, D.P. & Ramsey, L.W. 1987, ApJ, 319, 392
Kelch, W. L., Linsky, J. L., & Worden, W. P., 1979, ApJ, 229, 700
Kurucz, R. L., 1992, Rev. Mex. Astron. Astrof., 23, 45
Lites, B. W., Skumanich, A., Rees, D. E., Murphy, G. A., & Carlsson, M., 1987, ApJ, 318, 930
422, 351
Mihalas, D., 1978, Stellar Atmospheres, 2$^{\rm nd}$ ed., (W. H. Freeman and Co.)
Panagi, P. M., 1990, Ph. D. Thesis, Armagh Observatory
Short, C. I. & Doyle, J. G., A&A, 326, 287
Thatcher, J. D., Robinson, R. D., & Rees, D. E., 1991, MNRAS, 250, 14
Uitenbroek, H., 1989, A&A, 213, 360
Van Buren, D. & Young, A., 1985, ApJ, 295L, 39
Vogt, S. S., 1981, ApJ, 247, 975